JOURNAL OF SPACECRAFT AND ROCKETS
Vol. 45, No. 6, November–December 2008

Electric Propulsion and Controller Design for Drag-Free Spacecraft Operation

Paul Marchetti,* John J. Blandino,† and Michael A. Demetriou†
Worcester Polytechnic Institute, Worcester, Massachusetts 01609

DOI: 10.2514/1.36307

A study is presented detailing the simulation of a drag-free follow-up mission to NASA's Gravity Recovery and Climate Experiment. This work evaluates controller performance, as well as thrust, power, and propellant mass requirements for drag-free spacecraft operation at orbital altitudes of 160–225 km. In addition, sensitivities to thermospheric wind, Global Positioning System signal accuracy, and availability of ephemeris data are studied. Thruster (control actuator) models are based on two different Hall thrusters for providing the orbital along-track acceleration, colloid thrusters for the normal acceleration, and a miniature xenon ion thruster for the cross-track acceleration. At an altitude of 160 km, the maximum along-track thrust component is calculated to be 98 mN with a required dynamic (throttling) response of 42 mN/s. The maximum position error at this altitude was shown to be in the along-track direction with a magnitude of 3314.9 nm. At 225 km, the maximum along-track thrust component reduces to 10.3 mN. The maximum dynamic response at this altitude is 4.0 mN/s. For the spacecraft point design considered with a propellant mass fraction of 0.18, the mission lifetime for the 160 km case was calculated to be 0.76 years. This increases 2.27 years at an altitude of 225 km.

Nomenclature

A, B, C, D, E, F	=	Hall thruster model polynomial coefficients
a	=	semimajor axis of orbit, km
$\mathbf{a}_d$	=	acceleration due to atmospheric drag, km/s^2
$\mathbf{a}_{\text{ns}}$	=	acceleration due to aspherical geopotential, km/s^2
$\mathbf{a}_T$	=	control acceleration vector, km/s^2
$\mathbf{B}$	=	coordinate transformation matrix
C_b	=	ballistic coefficient, kg/m^2
C_d	=	drag coefficient
c	=	drag parameter, km^{-1}
$\hat{c}$	=	adaptive estimate, km^{-1}
$\hat{c}_0$	=	initial adaptive estimate, km^{-1}
$\tilde{c}$	=	drag parameter error, km^{-1}
e	=	orbital eccentricity
i	=	inclination of orbital plane, deg
K_P	=	proportional gain matrix, s^{-2}
K_D	=	derivative gain matrix, s^{-1}
Kn	=	Knudsen number
m	=	spacecraft mass, kg
$(m_p)_0$	=	initial propellant mass fraction
$\dot{m}$	=	mass flow rate, mg/s
$\mathbf{r}_t$	=	actual position vector of proof mass, km
$\mathbf{r}_c$	=	actual spacecraft position vector, km
$\mathbf{r}_m$	=	measured spacecraft position vector, km
$\dot{\mathbf{r}}$	=	inertial velocity vector, km/s
$\ddot{\mathbf{r}}$	=	inertial acceleration vector, km/s^2
S	=	reference area, 0.96 m^3
$\mathbf{u}_v$	=	velocity unit vector
$\mathbf{u}_{v,m}$	=	measured velocity unit vector
V_d	=	discharge voltage of Hall thruster, V
$\mathbf{v}_c$	=	actual velocity vector of spacecraft, km/s
$\mathbf{v}_m$	=	measured velocity vector of spacecraft, km/s
Γ	=	adaptive gain
γ	=	secondary velocity error gain
$(\Delta_{\text{pos}})_0$	=	initial position error, m
ΔV	=	change in velocity, m/s
$(\Delta_{\text{vel}})_0$	=	initial velocity error, m/s
$\delta\mathbf{r}$	=	actual position error, m
$\delta\mathbf{r}_m$	=	measured position error vector, m
$\delta\dot{\mathbf{r}}$	=	velocity error, m/s
$\delta\ddot{\mathbf{r}}$	=	state acceleration error, m/s^2
$(\delta\mathbf{v}_m)_{\text{num}}$	=	calculated velocity error vector, m/s
$\boldsymbol{\varepsilon}_{\delta r}$	=	position error uncertainty vector, km
$\boldsymbol{\varepsilon}_{\text{pos}}$	=	spacecraft position uncertainty vector, km
$\boldsymbol{\varepsilon}_{\text{vel}}$	=	spacecraft velocity uncertainty vector, km/s
$\boldsymbol{\varepsilon}_{\text{TR}}$	=	thruster resolution vector, km/s^2
ζ	=	damping coefficient
θ	=	true anomaly, deg
$\lambda_{\min}(\cdot)$	=	minimum eigenvalue of a matrix
μ	=	Earth's gravitational parameter, km^3/s^2
ρ	=	atmospheric density, kg/m^3
Ω	=	right ascension of the ascending node, deg
ω	=	argument of perigee, deg
ω_n	=	natural frequency of simple harmonic oscillator, Hz
$\omega_\oplus$	=	angular velocity of Earth, rad/s

Presented as Paper 5166 at the 42nd AIAA/ASME/SAE/ASEE Joint Propulsion Conference and Exhibit, Sacramento, CA, 9–12 July 2006; received 21 December 2007; revision received 23 May 2008; accepted for publication 3 June 2008.

*Graduate Student, Mechanical Engineering Department, 100 Institute Road; currently Mechanical Engineer at Raytheon Company, Marlborough, Massachusetts. Student Member AIAA.

†Associate Professor, Mechanical Engineering Department, 100 Institute Road. Senior Member AIAA.

I. Introduction

DRAG-FREE spacecraft are opening a number of possibilities for measurement-based missions in the near future. In this context, the term "drag-free" refers to the continuous cancellation of external disturbances on the spacecraft, which contains an inertial sensor. This sensor may consist of a freely floating proof mass located within an instrumented housing designed to detect movement of the mass relative to the spacecraft around it. The spacecraft itself shields the proof mass from nonconservative forces such as atmospheric drag and solar radiation pressure. The spacecraft's controller continuously activates the propulsion system to keep itself centered on the floating proof mass, which ideally should only be subjected to gravitational forces. The resulting orbit is drag-free in the sense that the trajectory of the proof mass is only governed by gravitational potential. The motion of the proof mass(es) can therefore be used to determine the local gravitational field. Drag-free

control was first demonstrated on the U.S. Navy Triad spacecraft in 1972 [1,2], and with the ongoing developments in propulsion technology, drag-free missions are becoming much more feasible. Although more complex to implement, a drag-free sensor using proof masses as described will have improved sensitivity (lower acceleration noise) compared with a more conventional accelerometer-based system. This is a consequence of the inherently lower centering force (and lower noise) associated with a drag-free sensor.

NASA's Gravity Recovery and Climate Experiment mission (GRACE), launched in March 2002, consists of two three-axis-stabilized spacecraft flying 50–220 km apart in the same 88.5 deg inclination, 500 km orbit. The orbital eccentricity is a near circular 0.001 to minimize the density variation over the course of an orbit. Each GRACE satellite is in the shape of a trapezoidal cube and measures 1.942 m wide, 3.123 m long, and 0.72 m high. The mass of each satellite is approximately 487 kg and each have a predicted drag coefficient of 2.5. Although GRACE is not drag-free, the objective of the GRACE mission is to map the gravitational field of the Earth by measuring differences in position and velocity between the two spacecraft. A *K*-band microwave ranging instrument is used to measure these differences between the spacecraft to within 1 μm.

The success of GRACE has led to consideration of a possible follow-up mission in the near future. In particular, operation at a lower altitude would allow the sensor to operate in a stronger gravity field, improving sensitivity at the cost of increased drag. A possible follow-up mission to GRACE would likely use drag-free spacecraft to measure the Earth's gravity field, where atmospheric drag can be continuously compensated for, rather than measured and subtracted out of the data. Such a follow-up mission could greatly increase the accuracy of current gravity models and provide benefits for weather prediction, studying ice sheets and ocean currents, tracking changes in the solid Earth, and tracking water movement on and beneath the Earth's surface.

One option for the follow-up mission would consist of a two spacecraft formation, flying in the same near-polar orbit, as with GRACE. Like GRACE, the two satellites themselves are an integral part of the instrument. However, the follow-up mission could use a drag-free control system to remove nonconservative effects completely, increasing measurement sensitivity. The follow-up mission will most likely use a laser interferometer for ranging, rather than the microwave ranging system flown on GRACE, reducing instrument noise by 2 orders of magnitude. Ideally, the follow-up mission would fly at a much lower altitude, around 200 km, compared with the 500 km orbit of the GRACE satellites.

In this study, the dynamics of a drag-free spacecraft, similar to that of the possible GRACE follow-up mission, are modeled. Spacecraft dynamics include two-body gravity effects as well as higher-order perturbations such as J_2-J_6 nonspherical geopotential effects. The spacecraft dimensions and mass are assumed to be identical to that of the GRACE satellites. Atmospheric drag is represented using a coefficient-based model in which drag force is assumed to be proportional to the square of the spacecraft's velocity. A direct simulation Monte Carlo code was implemented to validate the analytical drag model by accurately determining the drag coefficient for the assumed geometry at a particular orbital condition. The propulsion controller is based on Lyapunov's methods and uses partial state feedback linearization to keep the spacecraft centered on its encaged proof mass, which is assumed to be located at the center of mass of the spacecraft. The control law uses an online, or adaptive, estimator to predict the drag acceleration imparted on the spacecraft, because drag force is unknown a priori. Parametric thruster models provide accurate estimates for thrust as a function of operating conditions (discharge voltage and flow rate for the Hall thrusters), power requirements, and mass consumption. Results focus on thrust and power requirements, thruster and controller performance, and sensitivities to various changes in input parameters and assumptions.

Previous work by St. Rock et al. [3] investigated the propulsion requirements for a drag-free spacecraft operating continuously in Earth orbit at altitudes of 150–450 km for a period of up to five years. For the candidate spacecraft mass and geometry considered, the authors calculated the required thrust envelope, maximum thruster dynamic response, and ΔV. The feasibility of several candidate thruster technologies was also evaluated. One restrictive assumption in this earlier work was the continuous availability to the controller of full-state data for the spacecraft. In addition, no uncertainty was assumed in either the state data for the spacecraft, the data from the inertial sensor, or the delivered thruster response. This study is an extension of the previous work in which a number of the limiting assumptions in the original model have been eliminated. A major improvement in the current model is a more accurate representation of the available control information. The time period between spacecraft position and velocity updates is now a variable, and the sensitivity of the controller performance to the delay in these updates is explored. In addition, uncertainty in the spacecraft state data, the data from the inertial sensor and the delivered thruster response, has been included to enhance the realism of the simulations. Finally, we have included specific thruster (controller actuator) models for the along-track, normal, and cross-track control and a ballistic coefficient which varies with mass consumption over the course of the mission. This allows for a better assessment of the importance of thrust level and specific impulse on the thruster selection for a multiyear mission.

II. Dynamics Modeling

A. Reference Frames

The two coordinate frames used in this study are the inertial geocentric-equatorial (GCI) and a satellite-centered rotating frame (*NTW*). The GCI reference frame is used to define the equations of motions, the state error inputs into the control law, and the calculated thrust accelerations. The *NTW* frame has its origin located at the center of mass of the floating proof mass, as shown in Fig. 1. The along-track, or tangential *T*, axis of this reference frame is collinear with the velocity vector of the satellite. The cross-track, or *W* axis, is perpendicular to the orbital plane and is parallel with the angular momentum vector of the orbit ($\mathbf{h} = \mathbf{r} \times \mathbf{V}$). The normal *N* axis is perpendicular to both the *T* and *W* axes ($\mathbf{W} = \mathbf{N} \times \mathbf{T}$). For a circular orbit, the *N* axis will coincide with the spacecraft's GCI position vector.

In this study, the spacecraft occupy orbits with a slight eccentricity (0.001), and so the *N* axis of the *NTW* frame is slightly out of alignment with the satellite's GCI position vector. Whereas the controller will calculate the required thrust acceleration in the GCI frame (based on the GCI state error inputs), the applied thrust will be reported in the local spacecraft body-fixed frame (assumed to coincide with the rotating *NTW* frame) to represent thruster mounting on the spacecraft.

B. Orbital Dynamics

In simulating the dynamics of the spacecraft, one must define the dynamics of the floating proof mass as well as the spacecraft in which it is housed. The dynamics of the proof mass are assumed to only be governed by the Earth's gravity. The equation of motion which describes the motion of the target, or proof mass, is shown as Eq. (1):

$$\ddot{\mathbf{r}}_t(t) = -\mu \frac{\mathbf{r}_t(t)}{\|\mathbf{r}_t(t)\|^3} + \mathbf{a}_{\mathrm{ns},t} \tag{1}$$

The vector, $\ddot{\mathbf{r}}_t(t)$ is a 3×1 vector representing the components of acceleration in the GCI frame. The solution of this equation, $\mathbf{r}_t(t)$, represents the trajectory of the proof mass, or "target spacecraft," which includes only a two-body gravitational acceleration term and perturbation due to the nonspherical geopotential $\mathbf{a}_{\mathrm{ns},t}$. The nonspherical acceleration terms are taken from a simplified model for the zonal harmonic (J_2-J_6) acceleration terms by Vallado [4]. Because the spacecraft itself shields the proof mass from atmospheric drag and other nonconservative forces that will affect its orbit, accelerations dues to such perturbations are not included in Eq. (1). Equation (2) describes the motion of the "controlled" spacecraft. It also includes a two-body gravitational acceleration term and perturbations due to the nonspherical geopotential $\mathbf{a}_{\mathrm{ns},c}$, atmospheric drag $\mathbf{a}_d(t)$, and a control thrust acceleration $\mathbf{a}_T(t)$:

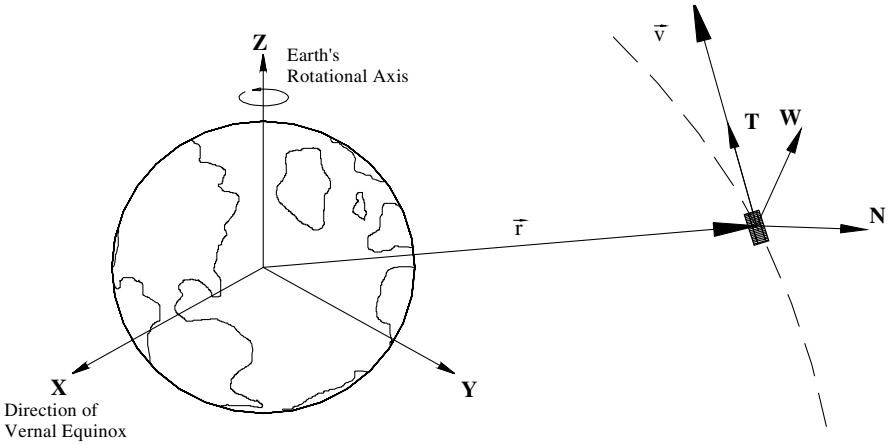

Fig. 1 Reference frames.

$$\ddot{\mathbf{r}}_c(t) = -\mu \frac{\mathbf{r}_c(t)}{\|\mathbf{r}_c(t)\|^3} + \mathbf{a}_{\text{ns},c} + \mathbf{a}_d(t) + \mathbf{a}_T(t) \tag{2}$$

The solution of Eq. (2) represents the trajectory of the controlled spacecraft $\mathbf{r}_c(t)$. The goal of the controller is to keep "errors" or differences in position and velocity of the target and the controlled spacecraft to a minimum. If these errors equal zero exactly, the spacecraft is said to be "centered" on the proof mass. The controller attempts to attain this desired state by sending a thrust signal to the actuator (thrusters) to produce a force which cancels the nonconservative forces (i.e., drag force) imparted on the spacecraft, represented by $\mathbf{a}_T(t)$ in Eq. (2). Because the drag force is an unknown quantity, the challenge of accurately estimating it is also part of the control objective. This is discussed in Sec. IV.

III. Drag Model and Monte Carlo Analysis

A. Drag Model

For this simulation, we use a drag model where the drag acceleration is proportional to the local density and the square of spacecraft velocity to describe the drag force imparted on the spacecraft by the Earth's atmosphere. The drag acceleration term in Eq. (2) is represented by

$$\mathbf{a}_d(t) = -\frac{1}{2}\left(\frac{C_d S \rho(t)}{m(t)}\right)\|\mathbf{v}_{\text{rel}}(t)\|^2 \frac{\mathbf{v}_{\text{rel}}(t)}{\|\mathbf{v}_{\text{rel}}(t)\|} \tag{3}$$

where $\mathbf{v}_{\text{rel}}$ is the velocity vector of the controlled spacecraft relative to the atmosphere. This includes the assumption that the atmosphere corotates with the Earth. The spacecraft mass $m(t)$ is time dependent and decreasing as propellant is consumed. The parameter S is the drag area of the spacecraft, or the normal projection of the spacecraft's cross-sectional area onto the NW plane. In the case of the GRACE spacecraft, the leading face is normal to the NW plane, so that the drag area is the spacecraft's cross-sectional area. The drag coefficient C_d is assumed to be 2.2 for each direction, a value which has been verified via direct simulation Monte Carlo (DSMC) analysis as presented in Sec. III.C. The quantity $\rho(t)[C_d S/2m(t)]$ is defined here as the *drag parameter* $c(t)$. This quantity is dependent on the two time-dependent parameters: atmospheric density and the mass of the spacecraft. By defining the relative velocity unit vector $\mathbf{u}_v(t)$, the drag acceleration can be written in the following compact form:

$$\mathbf{a}_d(t) = c(t)\mathbf{u}_v(t)\|\mathbf{v}_{\text{rel}}(t)\|^2 \tag{4}$$

B. Atmosphere Model

The drag model [Eq. (3)] assumes that the drag force imparted on the spacecraft is proportional to the local atmospheric density. Therefore, accurately modeling the drag forces depends heavily on the atmospheric density model used. In this study, the mass-spectrometer-incoherent-scatter (MSISE-90) atmosphere model is used [5]. Seven species are included in the model: O, O2, N, N2, Ar, He, and H (Table 1).

For this study, a density lookup table based on an altitude profile from 50–500 km, using 0.1 km intervals, was generated using 1 January 2000 as the reference date. Mass densities are then interpolated based on this lookup table for use in the simulation. This date was chosen because it is at the peak of the solar cycle, proving a "worst-case" scenario for solar activity.

C. Direct Simulation Monte Carlo Drag Analysis

For the altitudes considered in this study, 160, 200, and 225 km, the local mean free paths range from 20–30 m for the 160 km orbit to 200–270 m for the 225 km orbit. This corresponds to a Knudsen number on the order of 10 for the 160 km case. For the 225 km case, the Knudsen number increases to a few hundred. These values are in good agreement with previous work by Gatsonis et al., in which a DSMC analysis was performed to investigate pressure measurements made by a suborbital vehicle upon reentry [6]. Because of the high Knudsen numbers associated with the freestream flow conditions at these altitudes, a particle approach must be taken in determining aerodynamic forces on the spacecraft at these altitudes.

For the current study, a drag analysis was performed using a three-dimensional, unstructured DSMC code developed by Chamberlin and Gatsonis [7]. Simulations were run for the minimum and maximum drag situations for 160, 200, and 225 km orbits.

For each simulation, particles of each species were loaded into the computational cells based on their number densities. The injection

Table 1 Mass densities and neutral temperature

Orbital altitude, km	Drag case	Actual altitude, km	Velocity, km/s	Mass density, kg/m^3 ($\times 10^{-10}$)	Neutral temperature, K
160	Max	159.8092	7.8025	13.8	736.5
160	Min	168.7551	7.8014	9.48	770.3
200	Max	199.7617	7.7788	3.12	840.1
200	Min	208.6745	7.7776	2.358	851.3
225	Max	224.732	7.7641	1.467	865.7
225	Min	233.625	7.7629	1.142	871.3

Table 2 DSMC results

Orbital altitude, km	Min drag, N	Max drag, N
160	0.0691	0.0820
200	0.0148	0.0195
225	0.0071	0.0085

boundary conditions were defined to be a freestream uniform flow with magnitude equal to that of the spacecraft's velocity. All other domain boundaries were defined to be free boundary, meaning particles are free to move into and out of the domain. All spacecraft surfaces were assumed to be diffuse reflecting and in thermal equilibrium with the atmosphere. The results of the DSMC analysis are presented in Table 2.

An estimate of spacecraft drag coefficient could be determined from the DSMC results. Using Eq. (3) and the drag forces obtained from DSMC, the spacecraft drag coefficient can be solved for. In each case presented, this procedure was executed and the results were averaged. The average value of the drag coefficient based on the DSMC results was determined to be 2.2.

IV. Propulsion Controller Design

A. Continuous Full-State Controller

The dynamic Eqs. (1) and (2) can be combined and written in terms of the difference in states (i.e., the state acceleration error) as follows:

$$\delta\ddot{\mathbf{r}}(t) = \ddot{\mathbf{r}}_c(t) - \ddot{\mathbf{r}}_t(t) = \mu\left(\frac{\mathbf{r}_t(t)}{\|\mathbf{r}_t(t)\|^3} - \frac{\mathbf{r}_c(t)}{\|\mathbf{r}_c(t)\|^3}\right) + \mathbf{a}_d(t) + \mathbf{a}_T(t) \tag{5}$$

where the differential, nonspherical Earth acceleration goes to zero (i.e., $\mathbf{a}_{\mathrm{ns},t} = \mathbf{a}_{\mathrm{ns},c}$). This assumption is valid if the state errors are kept small and the proof mass is positioned at the center of mass of the satellite. The proposed control strategy uses partial state feedback linearization to cancel the nonlinearities in Eq. (5). This controller architecture minimizes the complexity of the adaptive scheme for estimating the drag acceleration $\mathbf{a}_d(t)$. With such a controller choice, the resulting closed-loop system consists of linear error dynamics (vector second-order system) and a linearly parameterized term due to the adaptive estimate of the drag acceleration. A more traditional control approach would have resulted in a nonlinear closed-loop system requiring a complex adaptive scheme for the drag estimate.

It is desirable to choose the control acceleration term in Eq. (5) so that it would cancel the nonlinear terms and the drag acceleration term. Such a control law is shown in Eq. (6):

$$\mathbf{a}_T(t) = -\mu\left(\frac{\mathbf{r}_t(t)}{\|\mathbf{r}_t(t)\|^3} - \frac{\mathbf{r}_c(t)}{\|\mathbf{r}_c(t)\|^3}\right) - [K_P]\delta\mathbf{r}(t) - [K_D]\delta\dot{\mathbf{r}}(t) - \hat{c}(t)\mathbf{u}_v(t)\|\dot{\mathbf{r}}_c(t)\|^2 \tag{6}$$

This control law was defined in previous work and assumes full-state availability with no uncertainty in any of the controller inputs or thruster response [3]. Later, this control law will be adapted to the case where the control inputs are discrete, have a prescribed uncertainty associated with each of them, and also include thruster repeatability in the control acceleration. The proportional and derivative gain matrices K_P and K_D, respectively, are 3×3 diagonal matrices and the control signal $\mathbf{a}_T(t)$ represents components of acceleration in the GCI frame needed to cancel the estimated drag on the spacecraft. Because the value of the drag parameter is not known a priori, the $\hat{c}(t)$ term in Eq. (6) represents an adaptive estimate of the actual drag parameter used in Eq. (4). The adaptive estimate is calculated from the update law

$$\frac{\mathrm{d}}{\mathrm{d}t}\hat{c}(t) = -\Gamma[\gamma\delta\dot{\mathbf{r}}(t) + \delta\mathbf{r}(t)]^T\mathbf{u}_v(t)\|\dot{\mathbf{r}}_c(t)\|^2, \qquad \hat{c}(0) = \hat{c}_0 \tag{7}$$

where γ is the secondary velocity error gain, $\hat{c}_0$ is the initial guess of the drag parameter, which is assumed to be calculated onboard based on spacecraft position [from Global Positioning System (GPS)] and atmospheric density estimates (from tables or models loaded on the flight computer), and Γ is the adaptive gain. The state acceleration error equation can now be written as a vector second-order order system:

$$\delta\ddot{\mathbf{r}}(t) + [K_D]\delta\dot{\mathbf{r}}(t) + [K_P]\delta\mathbf{r}(t) = [\mathbf{a}_d(t) - \hat{c}(t)\mathbf{u}_v(t)\|\dot{\mathbf{r}}_c(t)\|^2] = [c(t) - \hat{c}(t)]\mathbf{u}_v(t)\|\dot{\mathbf{r}}_c(t)\|^2 \tag{8}$$

It can be shown, with the right choice of $[K_P]$ and $[K_D]$, that the solution of this equation for the closed-loop system goes to zero exponentially when the adaptive estimate of the drag parameter is equal to the actual value [i.e., the known parameter case $\hat{c}(t) = c(t)$].

B. Hybrid Continuous/Discrete Partial State Controller

This section describes a modified controller based on realistic assumptions about available quantities.

1. *Availability of Spacecraft Ephemeris Data*

On an actual spacecraft, GPS signals are often received at periodic intervals. To capture the effect of not having continuous GPS information available to the controller, we now consider a more realistic case. For a drag-free application, it is desirable to receive GPS updates as often as possible so that accurate thrust commands can be issued. On the GRACE follow-up, the spacecraft's position and velocity vectors will be available every 10 s. For this study, the update frequency for the GPS position and velocity is assumed to be the same. Section VII.B.3 covers the systems sensitivity to different update frequencies for the spacecraft's position and velocity. The vectors $\mathbf{r}_m$ and $\mathbf{v}_m$ represent the "measured" GPS position and velocity vectors, and are synonymous with $\mathbf{r}_c(t)$ and $\dot{\mathbf{r}}_c(t)$ in the continuous case.

In addition to GPS position and velocity from the GPS system, the position error, or difference between the spacecraft's position and the proof mass, can be derived from the gravitational reference sensor (GRS). The GRS, which will be demonstrated on NASA's Space Technology 7 mission, will use capacitive sensors to measure the separation between the floating metallic cube (proof mass) and its housing. The position error, denoted as $\delta\mathbf{r}_m$, is assumed to be measured more frequently than the GPS updates, because the measurement is done onboard the spacecraft. For the nominal case, it is assumed that this quantity is updated every 0.5 s, or at a sampling frequency of 2 Hz. With this quantity, the position vector of the proof mass can be reconstructed from these measured values by the relation

$$(\mathbf{r}_t)_m = \mathbf{r}_m - \delta\mathbf{r}_m \tag{9}$$

The velocity error, denoted as $\delta\dot{\mathbf{r}}(t)$ in Eq. (6), is a nonmeasurable parameter. Therefore, it must be estimated or calculated numerically onboard. As a first approach, numerical differentiation of the position error was used. Differentiation of the measured position error vector $\delta\mathbf{r}_m(t)$ is carried out via a second-order backward difference method based on the GRS sampling frequency. The numerical velocity error, denoted by $[\delta\mathbf{v}_m(t)]_{\mathrm{num}}$, is calculated by

$$[\delta v_m(t)]_{\mathrm{num}} = \frac{\mathrm{d}}{\mathrm{d}t}\delta r_m \approx \frac{3\delta r_m^i - 4\delta r_m^{i-1} + \delta r_m^{i-2}}{2\Delta t} \tag{10}$$

where Δt denotes the time delay between GRS updates, 0.5 s. The quantity $[\delta v_m(t)]_{\mathrm{num}}$ will be used in place of $\delta\dot{\mathbf{r}}(t)$ in the control law, Eq. (6), and update law, Eq. (7). On the actual spacecraft, a more advanced method of estimating this value will mostly likely be employed, such as a nonlinear Kalman filter. This requires a nonlinear state observer for the error system, Eq. (8), which uses the noise-corrupted output signal $\delta\mathbf{r}_m(t)$ to reconstruct the velocity error $\delta\dot{\mathbf{r}}(t)$ to be used in the control and adaptive laws, Eqs. (6) and (7), respectively. Related to that is the possibility of an adaptive observer, which combines both the state error and drag parameter estimates in a single observer.

2. Uncertainty in Measurement

In addition to incorporating a time delay on the GPS position and velocity updates and the GRS position error update, the accuracy of these measurements is also considered. The GPS position information is assumed to be accurate to ±50 m. The spacecraft velocity is assumed to be accurate to ±10 cm/s. The values of 50 m and 10 cm/s are assumed to represent a 1-σ uncertainty in the position and velocity data, and are based on data from GRACE comparing the GPS velocity and the actual (postprocessed) velocity. In the simulation, these quantities are modeled by adding an error vector to the actual state, which is available from the solution vector of simulation, shown in Eqs. (11) and (12):

$$\mathbf{r}_m = \mathbf{r}_c + \boldsymbol{\varepsilon}_{\text{pos}} \tag{11}$$

$$\mathbf{v}_m = \mathbf{v}_c + \boldsymbol{\varepsilon}_{\text{vel}} \tag{12}$$

The uncertainty vectors $\boldsymbol{\varepsilon}_{\text{pos}}$ and $\boldsymbol{\varepsilon}_{\text{vel}}$ are 3×1 vectors consisting of the assumed 1-σ uncertainty value, multiplied by a random number vector on the interval $[-1, 1]$. The elements of the uncertainty vectors will therefore always consist of a value within ±1-σ selected with equal probability. These uncertainty vectors are generated at every update of the GPS position and velocity vectors.

The 1-σ GRS position error $\delta\mathbf{r}_m$ is assumed to be accurate to 5 nm. This quantity is modeled by adding an uncertainty vector to the difference of the spacecraft position vector and the target (proof mass) position vector, in a manner analogous to that described previously for the spacecraft position and velocity. The expression used to calculate the GRS position error is shown in Eq. (13) and is generated at the GRS sensing rate:

$$\delta\boldsymbol{r}_m = \delta\boldsymbol{r} + \boldsymbol{\varepsilon}_{\delta r} = (\boldsymbol{r}_c - \boldsymbol{r}_t) + \boldsymbol{\varepsilon}_{\delta r} \tag{13}$$

The three measured vectors $\mathbf{r}_m(t)$, $\mathbf{v}_m(t)$, and $\delta\mathbf{r}_m(t)$, and $[\delta\mathbf{v}_m(t)]_{\text{num}}$, are sent to the controller as they become available. In between updates, the control law uses the most recent value. At the start of a simulation, initial spacecraft position error $(\Delta_{\text{pos}})_0$ is set to its maximum uncertainty, 5 nm. The initial velocity error $(\Delta_{\text{vel}})_0$ is assumed to be zero, because the proof mass will be secured until it is "released" at the start of data collection on the actual mission.

3. Control Law

Measured values for spacecraft position $\mathbf{r}_m(t)$ and velocity $\mathbf{v}_m(t)$, and the position error $\delta\mathbf{r}_m(t)$, can be directly substituted for $\mathbf{r}_c$, $\dot{\mathbf{r}}$, and $\delta\mathbf{r}$ in Eq. (6) from data provided by the GPS and GRS systems. The calculated velocity error $[\delta v_m(t)]_{\text{num}}$ is substituted for $\delta\dot{\mathbf{r}}(t)$. Rewriting the control law in Eq. (6) in terms of these available quantities, the resulting control law is

$$\mathbf{a}_T(t) = -\mu\left(\frac{\mathbf{r}_m(t) - \delta\mathbf{r}_m(t)}{\|\mathbf{r}_m(t) - \delta\mathbf{r}_m(t)\|^3} - \frac{\mathbf{r}_m(t)}{\|\mathbf{r}_m(t)\|^3}\right) - [K_P]\delta\mathbf{r}_m(t) - [K_D][\delta\mathbf{v}_m(t)]_{\text{num}} - \hat{c}(t)\mathbf{u}_{v,m}(t)\|\mathbf{v}_{\text{rel},m}(t)\|^2 + \boldsymbol{\varepsilon}_{TR} \tag{14}$$

where

$$\mathbf{u}_{v,m}(t) = -\frac{\mathbf{v}_{\text{rel},m}(t)}{\|\mathbf{v}_{\text{rel},m}(t)\|} \tag{15}$$

and the quantity

$$-\mu\frac{\mathbf{r}_m(t) - \delta\mathbf{r}_m(t)}{\|\mathbf{r}_m(t) - \delta\mathbf{r}_m(t)\|^3}$$

represents the estimated gravitational acceleration on the proof mass based on the available information about the GCI spacecraft position and position error vectors. The last term in the control acceleration equation, $\boldsymbol{\varepsilon}_{\text{TR}}$ represents the thruster resolution, or uncertainty in thrust repeatability. Because thrusters are mounted directly to the spacecraft, the components of $\boldsymbol{\varepsilon}_{\text{TR}}$ are defined in the *NTW* frame and transformed into the inertial frame via the transformation matrix $\mathbf{B}$. The expression for $\boldsymbol{\varepsilon}_{\text{TR}}$ is shown in Eq. (16):

$$\boldsymbol{\varepsilon}_{\text{TR}} = \mathbf{B}\begin{bmatrix}\varepsilon_{\text{TR},N}\\ \varepsilon_{\text{TR},T}\\ \varepsilon_{\text{TR},W}\end{bmatrix} \tag{16}$$

The values for thruster repeatability uncertainty components will depend on the choice of thruster, feed system, and power processing unit. These issues will be discussed in Sec. V, Thruster Modeling. In addition, to accurately represent the thruster's capability, a thrust limiter has been implemented. In the case where the required control acceleration exceeds the capabilities of the assumed thruster model, the control acceleration is defaulted to the maximum acceleration the assumed thruster can deliver based on the mass of the spacecraft.

The adaptive estimate update law, Eq. (7), is also rewritten in terms of the known quantities and is shown in Eq. (17):

$$\frac{\mathrm{d}}{\mathrm{d}t}\hat{c}(t) = -\Gamma\{\gamma[\delta\mathbf{v}_m(t)]_{\text{num}} + \delta\mathbf{r}_m(t)\}^T\mathbf{u}_{v,m}(t)\|\mathbf{v}_{\text{rel},m}(t)\|^2 \qquad \hat{c}(0) = \hat{c}_0 \tag{17}$$

The adaptive update law, Eq. (17), is assumed to be solved onboard the spacecraft at the same sampling frequency as the $\delta\mathbf{r}_m(t)$ update, 2 Hz. The control law, Eq. (14), and the adaptive estimate update law, Eq. (17), describe the propulsion controller for the drag-free simulation.

Assuming the nonlinearities are cancelled out from Eq. (5) by use of the control law, Eq. (14), and if $\hat{c}(t) = c$, the result is a linear proportional-derivative-type controller. By proper choice of the proportional and derivative gain matrices, $[K_P]$ and $[K_D]$, one can ensure that the state errors will go to zero exponentially with a prescribed rate. The standard form of a second-order linear system is given by

$$\ddot{r}_i + 2\zeta\omega_n\dot{r}_i + \omega_n^2 r_i = 0 \qquad i = x, y, z \tag{18}$$

Therefore, the gain coefficient for this linear controller can be found from this expression. The gain matrices are then defined as diagonal matrices with the following values on the diagonal:

$$k_p = \omega_n^2, \qquad k_d = 2\zeta\omega_n \tag{19}$$

The natural frequency, as a controller design parameter, was chosen to be 0.999 Hz, slightly less than half of the update frequency (2 Hz) of the GRS position error. The damping ratio was chosen to be equal to 1.0, as was the one that provided better convergence of the parameter $\hat{c}(t)$. The secondary velocity error gain γ was chosen based on a stability analysis presented in [3] and is given by

$$\gamma > \max\left\{1, \frac{1 - \lambda_{\min}[K_D]}{\lambda_{\min}[K_P]}, \frac{1}{\lambda_{\min}[K_D]}\right\} \tag{20}$$

where $\lambda_{\min}$ represents the minimum eigenvalue of a matrix. The adaptive gain [8] Γ was chosen via an iterative process while tuning the controller. A summary of the control parameter values used in the simulation are shown in Table 3.

Table 3 Control parameters for simulations

Parameter	Value
γ	1.0001 s
Γ	1.2×10^{-4} s^{2}m^{-3}
ζ	1.0
ω_n	0.999 s^{-1}
k_p	0.998 s^{-2}
k_d	1.998 s^{-1}

V. Thruster Modeling

For the mission considered, where the propulsion system is continuously used to counteract drag forces, it is essential the thruster have a throttling capability. Because the orbit of the proposed follow-up mission has a slight eccentricity, density fluctuations caused by the spacecraft's periodic dipping into the lower atmosphere will be the driving factor in determining the throttling range of the thruster. For the lower altitudes considered in this study (160–200 km), a moderately powered (0.2–2.9 kW) Hall thruster was chosen for the along-track thruster model. For altitudes higher than 200 km, the required tangential thrust component is out of the range of the 0.2–2.9 kW candidate, therefore requiring a lower power thruster for these cases. A 200 W class experimental Hall thruster was chosen for this particular model. For the orbit normal thrusters, a colloid thruster model, based on the thrusters under consideration for the NASA Space Technology 7 (ST7) and Laser Interferometer Space Antenna (LISA) missions, was implemented, and a miniature xenon ion (MiXI) thruster model is used for the cross-track thrusters.

A. NASA/Aerojet 0.2–2.9 Kilowatt Hall Thruster Parametric Model

The along-track thruster performance modeling was partially based on experimental results of a 0.2–2.9 kW Hall thruster under development by NASA Glenn Research Center and Aerojet for NASA's *Discovery* science missions [9]. Several Hall thrusters have been designed for single set-point operation or with a moderate throttle-ability which may be used in orbit insertion and stationkeeping maneuvers. A 14:1 throttle range was demonstrated by the thruster described in [9] operating at a discharge voltage of 200–800 V. Anode mass-flow rate was varied between 1.3 and 3.6 mg/s for increased efficiency and thrust range. The demonstrated thrust range for this prototype thruster was 14.1–112.7 mN.

Experimental results from the *Discovery* mission thruster study were correlated to anode mass-flow rate and discharge voltage using a second-order polynomial least-squares multiple regression algorithm. The functional form of the correlation equations is shown in Eq. (21):

$$X = A + BV_d + CV_d^2 + D\dot{m} + E\dot{m}^2 + FV_d\dot{m} \tag{21}$$

where X is the parameter of interest. The parameters fit to this curve were thrust, total power (magnet power plus discharge electrical power), efficiency, discharge current, and specific impulse. Table 4 shows the coefficient values for the various thruster parameters. The accuracy of the curve fits, in terms of maximum percentage error, were as follows: thrust 8.97%, power 5.62%, current 7.10%, I_{sp} 6.23%, and efficiency 16.97%.

In this simulation, the acceleration command sent by the controller is converted to thrust, then used as the parameter X in Eq. (21), along with the coefficients A–F represented in Table 4. Given a thrust command from the controller, the resulting thrust equation is a second-order polynomial equation that can be solved for the corresponding discharge voltage, given a constant mass-flow rate of 3.6 mg/s. Once the flow rate and discharge voltage are known, other thruster parameters such as thrust, power, efficiency, discharge current, and specific impulse can then be calculated.

The thruster response uncertainty, as described in Sec. IV.B.3 was chosen for the along-track, or tangential, Hall thruster to be ±5% on the thrust command. This value represents the combined uncertainties in the feed system and power processor unit (PPU), as well as variations in the discharge plasma processes involved. The expression for the along-track thruster response acceleration uncertainty can be shown as

$$\varepsilon_{\mathrm{TR},T} = \frac{(T_t)(0.05)}{m}[\mathrm{rand}(-1, 1)] \tag{22}$$

where T_t is the commanded thrust, M is the spacecraft mass at that instant, and $[\mathrm{rand}(-1, 1)]$ is a random number, uniformly distributed, between -1 and $+1$, which provides the uncertainty range that is bounded by $\pm[(T_t)(0.05)]/m$.

B. NASA/Moscow Aviation Institute 90–250 Watt Hall Thruster Parametric Model

In addition to the NASA/Aerojet 0.2–2.9 kW Hall thruster, a lower powered Hall thruster was also modeled for simulations of higher orbits, where the required thrust profiles are out of the range of the larger thruster. Experimental results were taken from Jacobson and Jankovsky on a 200 W class Hall thruster between the power levels of 90–250 W [10]. The experimental data were fit using the same second-order multiple regression algorithm as used for the larger powered thruster, Eq. (21). The polynomial fit coefficients for the stationary plasma thruster (SPT-30) are shown Table 5.

The maximum errors in the polynomial fits of the 200 W class thruster data were 5.17% thrust error, 3.67% power error, 5.04% current error, 5.67% I_{sp} error, and 6.35% efficiency error. The thrust resolution uncertainty is assumed to be the same as the larger thruster, 5% of the commanded value, in accordance with Eq. (22).

C. Colloid Thruster Model

The controller thruster/actuator model for the normal direction thruster was based on data reported by Ziemer et al. [11]. That work summarizes performance goals and current technology status for colloid thrusters under development for the ST7 and LISA missions. For those missions, the performance requirements include a thrust range of 5–30 mN (0.5–6 mN per emitter) and a thrust resolution of 0.1 mN. The thrust-to-power ratio is projected to be 20 mN/W and does not include heaters, cathode neutralizer, or power supply losses.

Table 4 Polynomial fit coefficients for 0.2–2.9 kW Hall thruster

Parameter, X	A	B	C	D	E	F
Thrust, mN	−0.38001	0.029144	-5.1578×10^{-5}	0.25035	0.91899	0.038242
Total power, W	0.43338	−0.50878	0.00048	−8.2874	4.3917	1.006
Efficiency	0.036376	0.00135	-1.2897×10^{-6}	0.01970	−0.00189	6.0655×10^{-5}
Discharge current, A	0.2371	0.00142	-7.1085×10^{-7}	0.20944	0.16146	-8.2702×10^{-5}
Specific impulse, I_{sp}	85.845	4.3989	−0.00297	44.578	−17.436	0.40568

Table 5 Polynomial fit coefficients for 90–250 W Hall thruster

Parameter, X	A	B	C	D	E	F
Thrust, mN	−1.6432	0.018726	−0.00011	0.24133	−0.86076	0.07297
Total power, W	4.0061	−0.19193	0.000482	10.771	−9.0497	1.1119
Efficiency	−0.02541	0.001862	-6.76×10^{-6}	−0.0433	−0.07724	0.001686
Discharge current, A	0.19187	0.000299	-4.38×10^{-7}	0.34271	0.44079	0.000188
Specific impulse, I_{sp}	−32.32	5.1392	−0.01186	−50.027	−176.6	3.8823

At these altitudes, where a neutralizer may not even be required, these additional power drains were considered insignificant compared with the Hall thruster power. The specific impulse is 500–1500 s. In this study, we assume a constant specific impulse of 500 s for use in our calculations. For a 160 km drag-free mission, thrust in the normal and cross-track directions may exceed the 30 mN maximum described by Ziemer et al. for ST7 and LISA missions. If this is the case, either more thrusters would be needed, where some would remain on and others throttled to provide the necessary thrust, or a new thruster developed with a larger number of emitting needles. In this analysis, the colloid thruster(s) are assumed to be capable of delivering a desired thrust value to within ± 1 mN.

Unlike the model for the along-track Hall thrusters, it is assumed that, for this colloid model, the specific impulse is constant at 500 s. This represents the low end of the range of specific impulses this thruster configuration is capable of, but it will provide conservative estimates on propellant usage. The power required by the thruster(s) is calculated by dividing the commanded thrust by the thrust-to-power ratio.

D. Miniature Xenon Ion Thruster Model

A cross-track component of drag exists because of the corotation of the atmosphere with the Earth. For the altitudes considered, the maximum drag in the cross-track direction due to this effect ranges from about 0.5 mN at 225 km to about 4 mN at 160 km. The required thrust is therefore out of the range of a "typical" colloid thruster. NASA Jet Propulsion Laboratory has been developing a miniature xenon ion (MiXI) thruster designed for precision formation flying applications such as this [12]. The current MiXI thruster prototype will provide 0.5–3 mN of thrust at 3000 se specific impulse and efficiencies around 50% or better. The thrust-to-power ratio for this thruster is estimated to be 30 mN/W. The thruster response uncertainty for the MiXI thruster is assumed to be the same as the Hall system, or 5% of the commanded thrust value. This, again, is a result of uncertainties in the PPU and feed system for the ion thruster. Because the propellant is xenon, there is a system level benefit to using the MiXI with either of the aforementioned Hall thrusters, which also use xenon as a propellant.

VI. Simulation Details

The simulation code was written in MATLAB and assumes a spacecraft mass and geometry identical to GRACE, with the proof mass located as the center of mass of the spacecraft. The atmosphere model assumes that the atmosphere corotates with the Earth at an angular velocity of 7.292×10^5 rad/s. The argument of the perigee ω, right ascension of the ascending node Ω, true anomaly θ, and orbital inclination i have values of 45, 0, 180, and 88 deg, respectively.

The code integrates the dynamic equations of motion on the interval of one simulation time step and all control information is updated only when it becomes available. This results in constant control acceleration over the simulation time step, while all other orbital perturbations are dynamically governed by the solution of the differential equation of motion. This represents a realistic simulation of the actual spacecraft dynamics/control thrust relationship, because drag acts continuously on the spacecraft but the controller sends a thrust command at a discrete frequency. Thruster performance variables and propellant consumption is calculated at every simulation time step.

At the start of each simulation time step, initial conditions for that interval are defined for the target and controlled spacecraft dynamics from the final conditions of the previous step. As mentioned earlier, at the start of the simulation, the initial position error is set equal to its maximum uncertainty bound, 5 nm, with the initial velocity error set to zero. This corresponds to the initial displacement and velocity error when the proof mass is released after the spacecraft has been inserted into its desired orbit on the actual mission. The initial guess for the adaptive drag parameter estimate is calculated based on the altitude of the insertion point, and a density estimate is interpolated from the MSISE-90-generated lookup table. In the actual mission, the spacecraft will probably use a similar technique where the density is estimated using some algorithm if not provided by ground controllers.

VII. Results

Detailed results are presented for two different orbital altitudes: 160 and 225 km. The apogee of these orbits is roughly 9 km greater than the perigee (160 and 225 km) in both cases.

A. Mission Requirements and Lifetime

This section describes the thrust envelope, maximum dynamic thruster response, power requirements, and propellant consumption over the simulation time of two orbital periods for each of the altitudes presented. In each case, these results are extrapolated to provide estimates on mission lifetime and total power consumption for an extended mission. Figure 2 shows the required tangential thrust envelope for the range of orbital altitudes considered. The difference in maximum and minimum thrust values at each of the different orbital altitudes is mainly driven by density variations due to the slight eccentricity of the orbits. Larger orbital eccentricities would increase required thrust range. Because of the exponential nature of the atmospheric density with altitude, the lower altitude orbits display a much greater required thrust and thrust range.

Figure 3 shows the maximum thrust required for orbital altitudes from 160 to 500 km for each component in the spacecraft *NTW*

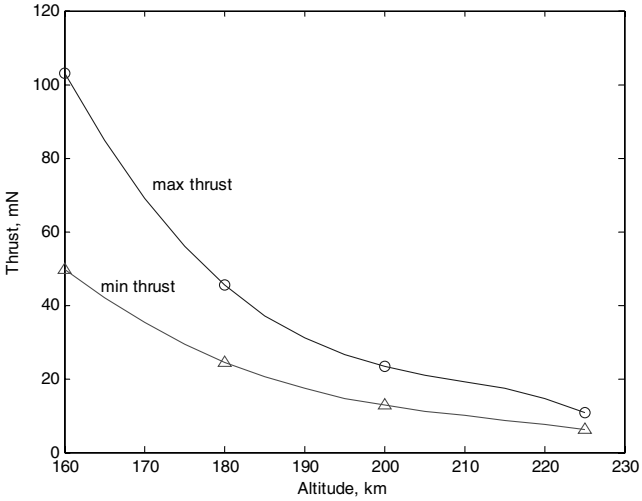

Fig. 2 Thrust envelope for 160–225 km.

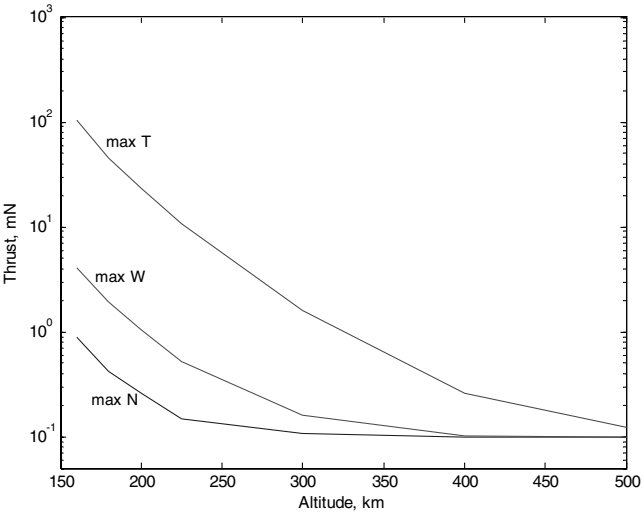

Fig. 3 Max thrust in *NTW* for 160–500 km.

coordinate system. For altitudes below ∼300 km, the maximum thrust components in the *N* and *W* directions are less than 10% of the maximum tangential thrust. Above ∼300 km, the effect of the corotating atmosphere becomes larger relative to the along-track *T* drag. At around the GRACE altitude of 500 km, the required thrust for the normal and cross-track directions is of the same magnitude, and the along-track thrust requirement is slightly greater. This suggests the need for fewer thruster types onboard the spacecraft, which may be advantageous from a system's standpoint. For the altitudes considered in this study, the magnitude of the required thrust in each spacecraft direction requires different types of thrusters to optimally provide the needed force.

For a 160 km orbit, the along-track *T* drag force imparted onto the spacecraft varies from 60.75 to 88.78 mN. The cross-track *W* drag force varies from −3.89 to 4.33 mN. The drag force profile for each of the *NTW* directions over two orbital periods is shown in Fig. 4. Figure 5 shows the applied thrust in all three *NTW* directions in response to this imparted drag. For the along-track direction, the thrust varies between 54.49 and 98.22 mN, and for the cross-track direction, it varies between −4.82 and 4.37 mN. As mentioned in the modeling section, the along-track thruster is assumed to be the NASA/Aerojet 02.–2.9 kW Hall thruster for all orbital altitudes except for 225 km, in which case the NASA/RIAME (Research Institute of Applied Mechanics and Electrodynamics of the Moscow Aviation Institute) thruster is used. The peak-to-peak difference in maximum and minimum along-track and cross-track thrust is slightly greater than that of the drag profile, due to controller error and uncertainty in the applied thrust values. Although no external perturbation is modeled directly in the *N* direction, normal direction state errors accumulate from the tangential drag force and the corotating atmosphere, which cause a control response resulting in a thrust command. The cross-track direction shows the majority of the crosswind disturbance due to the atmosphere corotating with the angular velocity of the Earth. Because the orbital inclination is near polar (88.5 deg), this effect results in additional drag force which is almost purely in the cross-track direction. The cross-track direction thrust changes sign twice during the course of one orbital period. However, the thrust force in the *N* direction changes sign over much shorter time scales (a few seconds in this case), and the problem of delivering the commanded thrust becomes apparent. Because of these factors, thruster mounting becomes an important issue for the spacecraft to be able to deliver the needed thrust in opposing directions. One solution is to mount opposing thrusters on each side of the spacecraft and assign all positive thrust commands to the positive thruster and all negative thrust commands to the negative thruster.

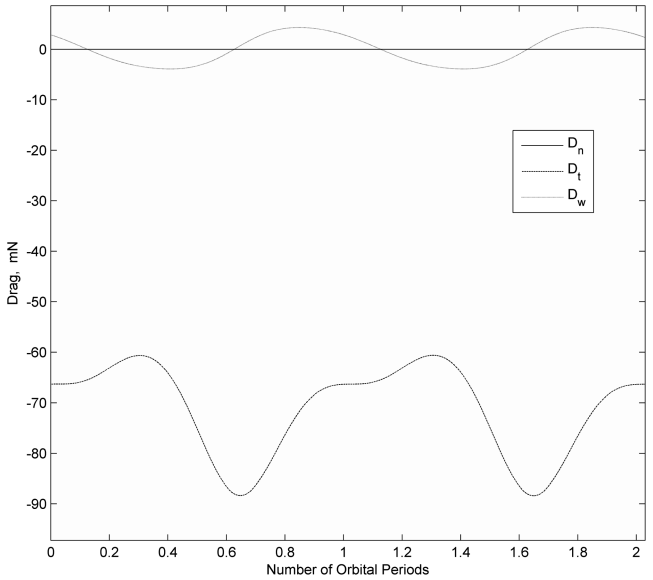

Fig. 4 Drag force profile for 160 km.

The problem with this configuration is that all opposing *N* and *W* direction (colloid and MiXI) thrusters will need to be required to be activated and deactivated repeatedly. The MiXI or *W* direction thrusters would most likely be able to handle this duty cycle, because they would only be required to activate once per orbital period, for a time of about half of an orbital period, or roughly 45 min. In the *N* direction, this thruster activation would need to occur over a time scale of a few seconds. Colloid thrusters are not usually designed for this type of "pulsed" operation and may not perform well. Pulsed-plasma thrusters may be a good alternative if the pulse time and thrust repeatability can be controlled effectively. Another more feasible option would be to use the colloid thruster configuration as described previously, with the addition of a set threshold value that the

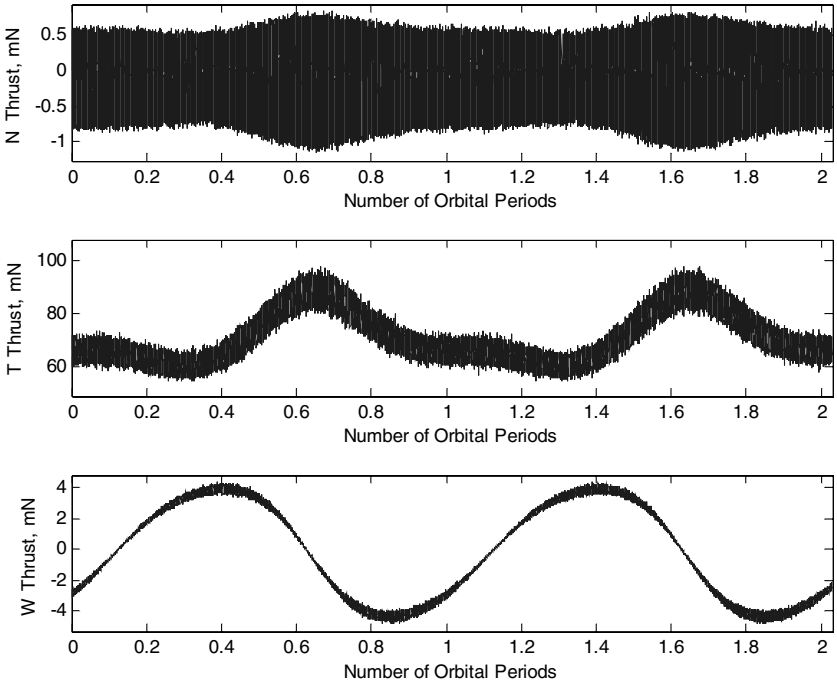

Fig. 5 *NTW* thrust component profiles for 160 km.

nonactive thruster defaults to when the thrust command is in the opposite direction. This would require the active thruster to produce the commanded thrust, plus the threshold value, to produce a resultant thrust force of exactly the commanded value. This split configuration allows all four N and W direction thrusters to fire continuously, only throttling between the commanded value plus the threshold, and the threshold value itself. This configuration will consume more propellant, because all thrusters are firing continuously, but the smoother operation will help in keeping state errors small, which in turn will produce more efficient thrust commands from the controller.

In the along-track, or T direction, the Hall thruster is primarily continuously throttled to counteract atmospheric drag. Because the magnitude of the drag force is much greater than zero, the short time-scale variation of the force does not require a sign change, as it does in the N and W directions. The factors which drive the choice of an appropriate thruster are the thrust range, which can be extreme for higher eccentricity orbits, and the maximum dynamic thrust response, which is driven mainly by the short time-scale variations. For the 160 km orbit, the maximum thruster response was 41.63 mN/s. Thruster response was calculated by numerical differentiation of the thrust profile with respect to time. From this, the maximum rate of change in thrust response is found. The maximum dynamic response of the along-track direction was found to be 41.63 mN/s, whereas the N and W directions displayed values of 2.18 and 2.44 mN/s, respectively.

The power required for each thruster is shown in Fig. 6. The majority of the power consumption is due to the Hall thruster, peaking at a value of 2223 W. The total power requirement for 160 km peaks at 2331 W. At this altitude, the mass-flow rate to the Hall thruster was chosen to be 3.6 mg/s, the maximum value assumed for the particular thruster.

For a drag-free mission, the state errors should be kept as small as possible. At 160 km, the state errors are the largest of the cases considered and may be a limiting factor in mission design. The displacement and velocity errors are shown in Figs. 7 and 8. Maximum values for the N, T, and W position errors are 1819.5, 3314.9, and 206.0 nm, respectively. Maximum velocity errors are 1037.5, 6384.7, and 331.7 nm/s for the N, T, and W directions.

At 225 km altitude, the drag force is significantly reduced as compared with the lower altitude case. The range of along-track drag force is 7.26–9.33 mN. The applied thrust profile ranges from 6.49 to 10.30 mN in the along-track direction. The maximum dynamic thruster response for this direction is 3.98 mN/s, significantly lower than any of the previous, lower altitude cases. Maximum dynamic responses for the N and W directions are 0.44 and 0.38 mN/s, respectively.

The maximum power required for a 225 km orbit is 234 W. Note that, for this altitude, the smaller, NASA/RIAME 90–250 W Hall thruster model is employed in the along-track direction. The Hall thruster mass-flow rate for this thruster and altitude combination is 0.98 mg/s. Even at this altitude, the majority of the required power is due to the Hall thruster power requirement, but the cross-track drag component is a larger contributor relative to the along-track drag than the previous cases, contributing roughly 20% of the total power.

At 225 km altitude, the state errors are reduced on the order of a few hundred nanometers. Maximum values for the N, T, and W position errors are 199.5, 367.9, and 34.5 nm, respectively. Maximum velocity errors are 157.3, 672.6, and 76.7 nm/s for the N, T, and W directions.

Using the mass consumption estimates provided by the thruster models, an estimate of feasible mission lifetime can be recovered. As a baseline for comparison, 87 of the 487 kg of the spacecraft's initial wet mass is assumed to be propellant mass. This equates to an initial propellant mass fraction of 0.18. Mission lifetime estimates are based on calculating how long it would take the spacecraft to expend 87 kg of propellant. The mass consumption rates for altitudes of 160–225 km are 0.0216, 0.0155, 0.0117, and 0.0065 kg/orbit, respectively. Figure 9 summarizes the estimated mission lifetime for an orbital altitude of 160–225 km based on the mass consumption rates listed.

Figure 10 shows the projected mission lifetime for a range of initial mass fractions from 0.1 to 0.5. The plot shows that, for a low-altitude drag-free mission, a five-year lifetime is likely not feasible. However, at 225 km, a five-year mission could be achieved if the initial propellant mass were roughly 0.38, for a 487 kg spacecraft, which equates to an initial propellant mass of 185 kg.

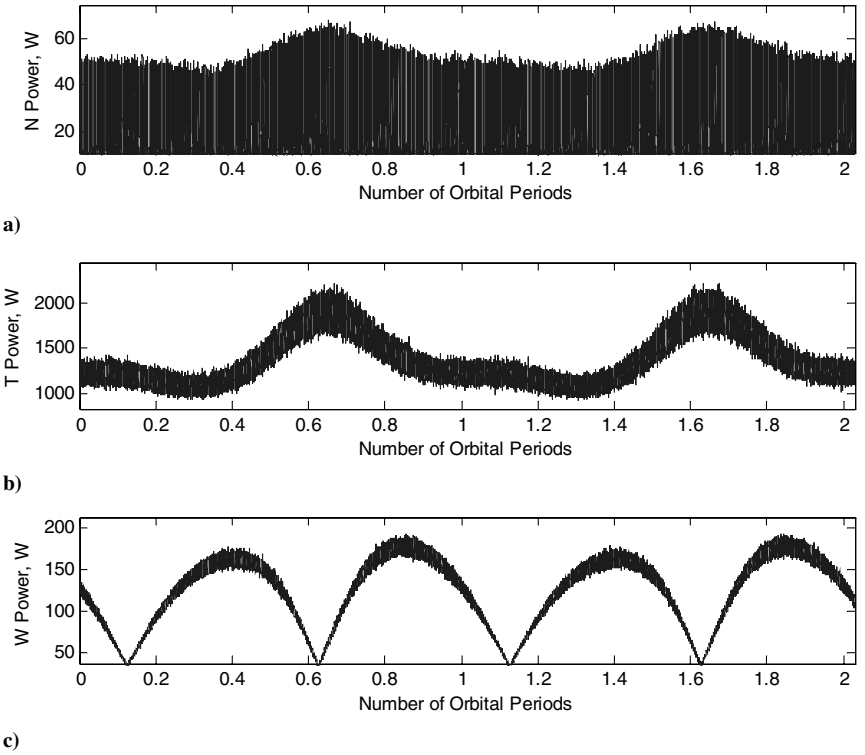

Fig. 6 Power requirements: a) N (colloid) power vs time, b) T (Hall) power vs time, and c) W (MiXI) power vs time for 160 km.

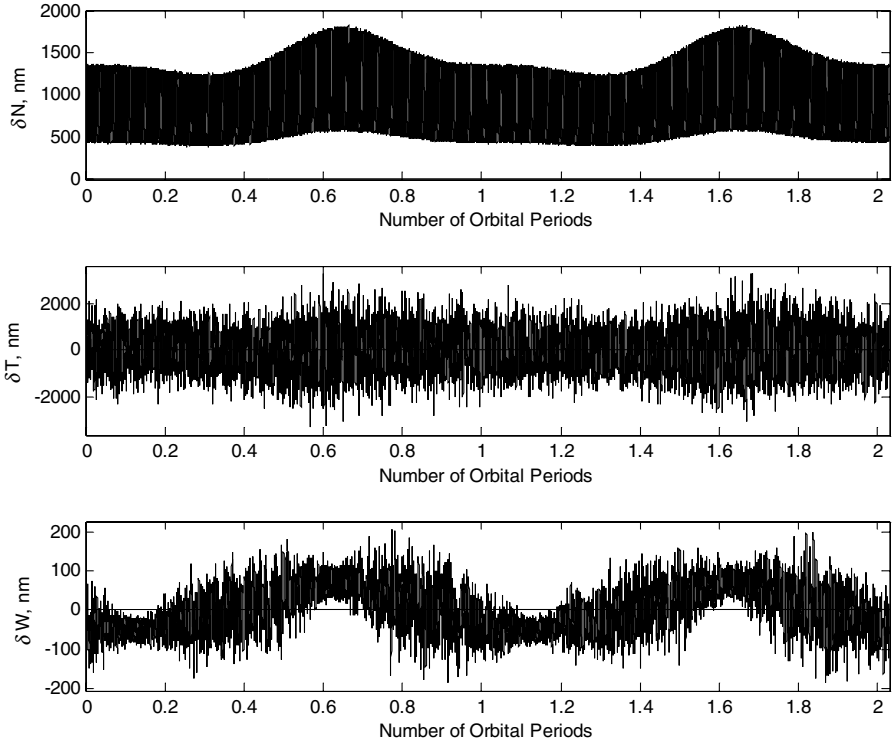

Fig. 7 Displacement errors for 160 km.

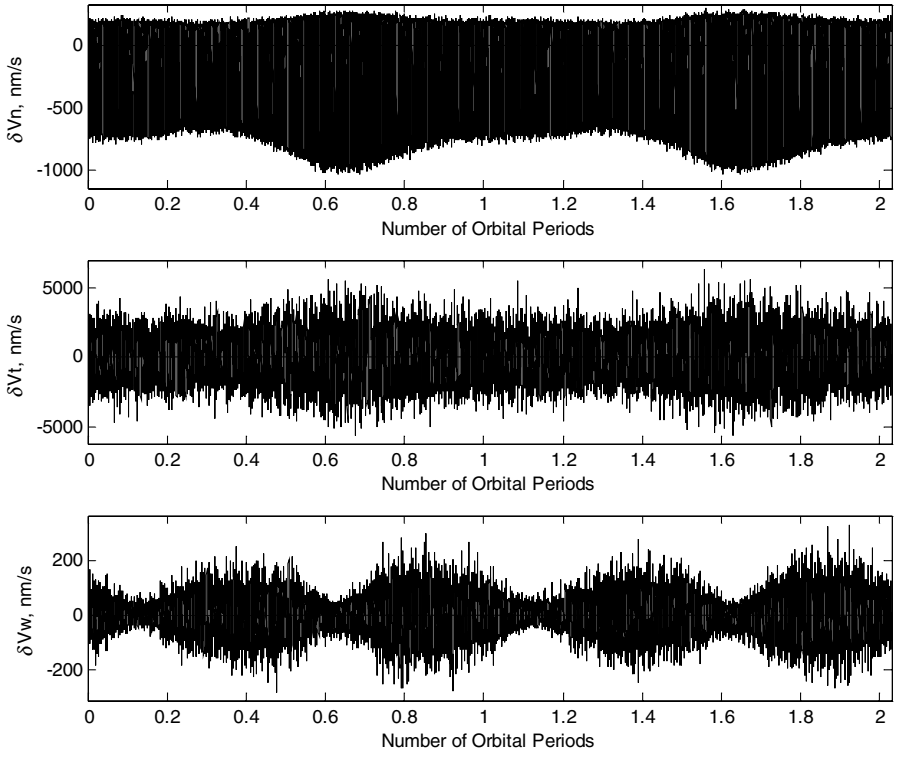

Fig. 8 Velocity errors for 160 km.

B. Sensitivities

This section describes the sensitivity of the system to various disturbances or changes in assumptions. First, the effect of adding a worst-case wind gust disturbance is evaluated. Second, we discuss the sensitivities of the system to changing two assumptions on the quality and frequency of two control inputs: the GPS position and velocity vectors. Note that the assumed update frequency and uncertainty of the GRS position error remains unchanged for this analysis. Sensitivity results for the various GPS assumptions are presented for the 225 km case only.

1. Effect of Thermospheric Wind

Other than the atmosphere corotating with the Earth, no additional wind disturbance has been included in the dynamic model. Winds in the lower thermosphere (90–200 km) can be significant, however, and should be addressed to determine a more robust estimate on propulsion requirements of a drag-free mission at these altitudes. Thermospheric winds were measured during a geomagnetic storm on 4–5 April 1993 by the Wind Imaging Interferometer (WINDII) between 90 and 200 km altitude, and 20–70 deg south latitude [13]. The WINDII instrument recorded a maximum wind velocity of

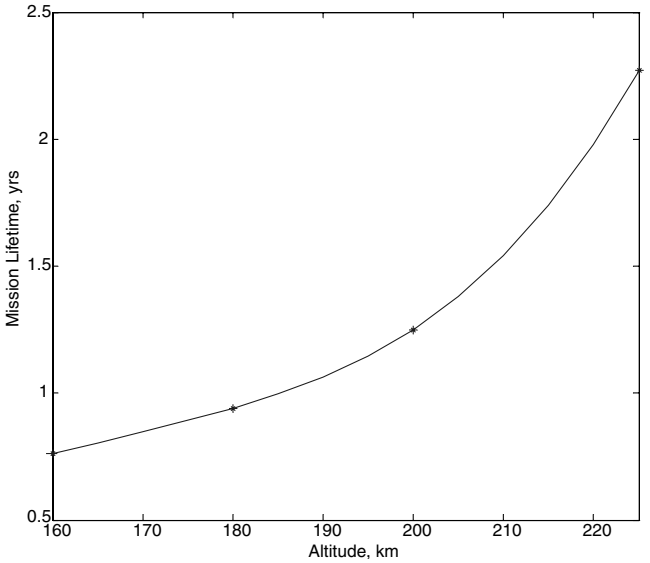

Fig. 9 Estimated mission lifetime for initial propellant mass fraction of 0.18.

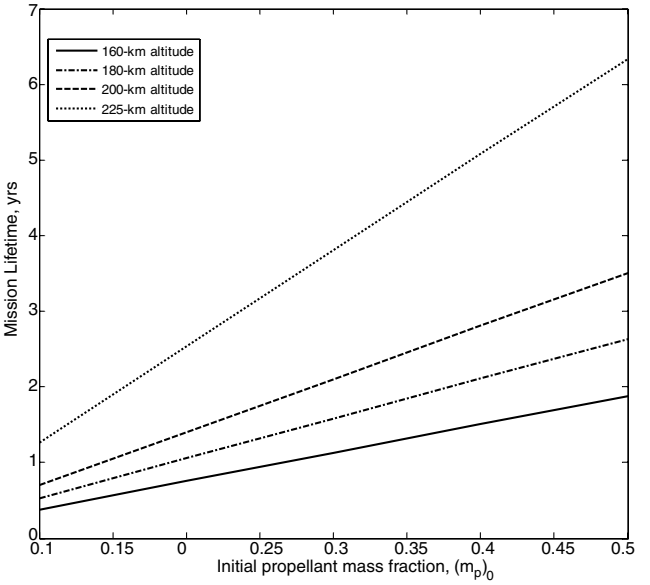

Fig. 10 Estimated mission lifetime for various initial mass fractions.

$\sim$200 m/s on 2 April at an altitude of 140 km. On 5 April, the maximum wind velocity was reported to be $\sim$650 m/s in the westward direction at an altitude of $\sim$200 km. To estimate the effect of such a wind on a drag-free mission, an impulsive gust of 650 m/s was modeled and implemented in the cross-track direction at 200 km. In addition to capturing the worst-case direction for the wind gust (westward), the geographic location of the wind measurement was taken into account in determining the time coordinate during the orbital period of the spacecraft when the gust occurred. Based on results reported by Zhang and Shepherd [13], the maximum winds were recorded in the southern polar region. This occurs close to the spacecraft's perigee as the spacecraft passes over the South Pole region.

The wind gust model implemented in the simulation assumes a Gaussian velocity profile in time where the time of the maximum wind gust was defined to be 3210 s, with a maximum velocity of 650 m/s and a duration of 6 s. As mentioned, to represent the worst-case scenario, this wind gust is injected in the W, or cross-track direction, because the effect of such a wind gust will have a larger relative effect as opposed to the along-track direction, where form drag dominates. This also provides some insight into thruster

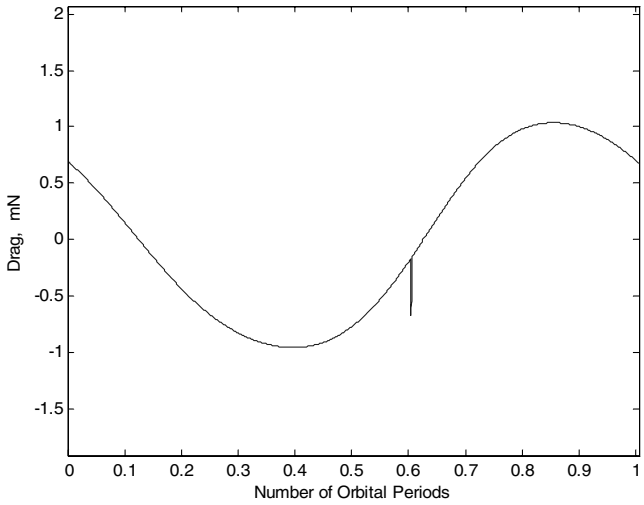

Fig. 11 Drag profile with worst-case wind disturbance in cross-track direction.

options, because the cross-track thrusters have been chosen largely based on the disturbance of the corotation of the atmosphere alone. The implementation of the wind gust is done by adding its velocity to the relative velocity of the spacecraft with respect to the atmosphere. The resulting drag force including the wind gust effect is found using the drag model defined by Eq. (5). The cross-track drag profile (including wind gust) for an altitude of 200 km is shown in Fig. 11. The effect of the wind disturbance can be seen around 0.6 of the orbital period.

Figure 12 shows the resulting thrust profile due to the additional wind disturbance. At 200 km, the worst-case effect of a strong wind gust increases the maximum required thrust in the cross-track direction from 1.12 to 2.01 mN, roughly a 79% increase. This disturbance results in a maximum dynamic thruster response in the cross-track direction of 0.61 mN/s, which is relatively unchanged from the nonwind disturbance case. This effect may be a significant consideration in choosing an appropriate thruster for the cross-track direction. For a 200 km orbit, the MiXI thruster should be capable of handling the larger thrust requirement, but lower altitude orbits may need more thrusters to deliver the needed thrust in the case of a large wind gust.

Such a disturbance also affects the state errors of the spacecraft. At 200 km, a 650 m/s gust causes the position error in the cross-track direction to increase to 860.4 nm. This large increase in the cross-track position error is quickly reduced as the control system recovers from the impulse disturbance, and the cross-track position errors return to the nominal values.

Again, this analysis represents a worst-case situation, where the maximum wind gust is short and intense, and the wind force imparted on the spacecraft is purely in the cross-track direction. Average wind speeds in the lower thermosphere during nongeomagnetic storm conditions are likely to be much less severe. Two days before the April 1993 storm, winds at 180 km in the polar cap were generally less than 200 m/s. For winds below 200 m/s, the choice of thrusters would only be stressed if a direct gust of 200 m/s were to occur at or near the maximum thrust, or about 0.4 orbital periods in Fig. 12.

2. *Effect of Global Positioning System Accuracy on State Errors*

To reduce state errors to minimum levels, the relative "error" or uncertainty in control inputs must also be reduced. We consider an improvement on the GPS position signal uncertainty from $\pm$50 to $\pm$1 m, and an improvement on the GPS velocity signal uncertainty from $\pm$10 to $\pm$1 cm/s. Table 6 shows the root mean square value δ_{rms} of the position error and the standard deviation σ_δ of the position errors for the nominal case, the improved accuracy cases, and the case of no uncertainty in the GPS signal.

It can be seen that significantly improving the accuracy of the GPS position and velocity signals do not drive a significant improvement

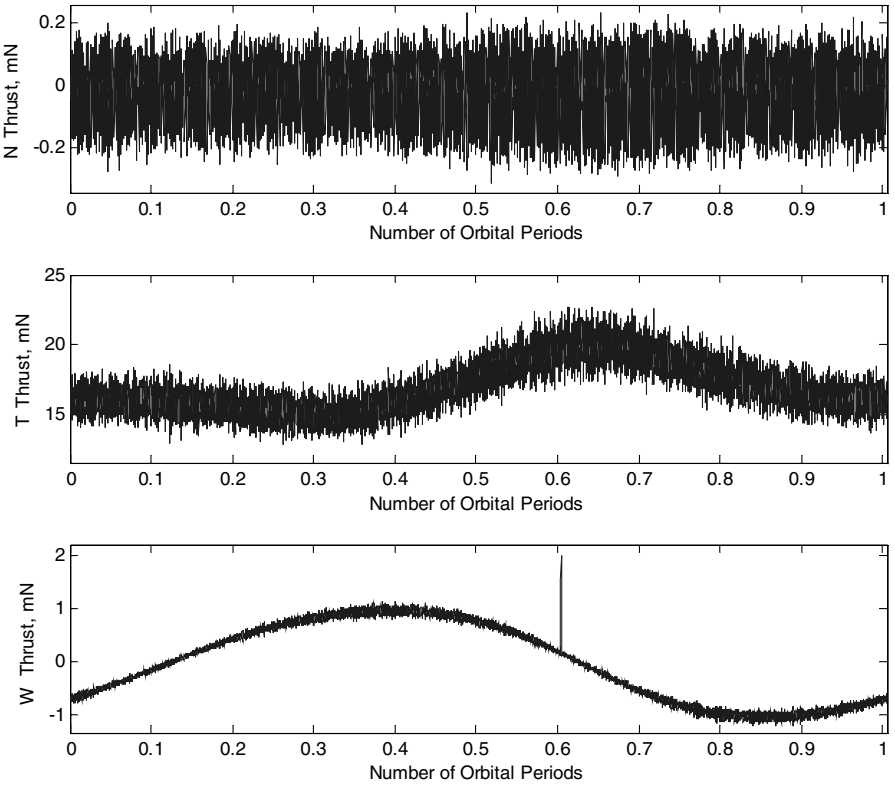

Fig. 12 ***NTW*** **thrust profiles with worst-case wind disturbance in cross-track direction.**

in the state errors of the system. This result may possibly be attributed to insufficient disturbance rejection of the controller and would therefore warrant further optimization of the controller parameters.

3. Effect of Global Positioning System Update Frequency on State Errors

In addition to considering the theoretical improvement of GPS signal quality, a decrease in the time delay between such updates is also examined. For this case, the original accuracy of GPS position and velocity signals is assumed. The time delay between GPS position and velocity updates is assumed to be reduced from 10 s in the nominal case to 1 s for this case. This allows the control algorithm to use more frequent updates of the spacecraft position and velocity to better estimate gravitational accelerations on the proof mass and drag accelerations on the spacecraft. Table 7 summarizes the results by presenting the maximum state errors for both the nominal case and the improved GPS update frequency case. It can be seen that the displacement error in the N direction is greatly reduced by the increase in update frequency. A reduction of over 80% is apparent for the N direction displacement error magnitude and a reduction of over 89% in the root mean squared (rms) value.

A decrease of over 28 nm is realized in the maximum along-track displacement error. The rms value in this direction shows an improvement of 0.979 nm, whereas the RMS cross-track displacement error is reduced by 1.27 nm. These results suggest that more frequent spacecraft position and velocity updates may help significantly reduce the displacement errors, thus keeping the spacecraft on the target trajectory.

VIII. Conclusions

A simulation of a possible drag-free GRACE follow-up mission is presented to evaluate the feasibility of such a mission at different orbital altitudes. The results presented in this paper suggest the feasibility of a drag-free mission in low-Earth orbit from the standpoint of the control algorithm and thruster actuators. However, limitations on maximum allowable state errors and thrust requirements may force the mission into higher orbital altitudes, where drag is not as severe. For the altitudes considered, required thrust range was shown to be mainly dependent on density fluctuations between apogee and perigee due to altitude changes. Therefore, given the choice of orbital eccentricity, a more circular orbit would be desired to reduce the peak-to-peak thrust variation between apogee and perigee. A 4–5% variation in altitude drives atmospheric density fluctuations causing the throttle envelope to be upward of 50% of the average thrust over an orbital period. For a 160 km orbit, the along-track thrust envelope was 54.3–98.5 mN, a throttle envelope of 44.1 mN. Higher altitude orbits require less maximum thrust as well as a narrower thrust envelope, thereby

Table 7 Effect of improved GPS accuracy on state errors

	Nominal, nm		Improved accuracy, nm	
Direction	δ_{rms}	σ_δ	δ_{rms}	σ_δ
N	103.48	35.441	11.317	5.4033
T	87.787	52.761	86.808	52.524
W	7.9557	4.6437	6.6823	4.108

Table 6 Effect of improved GPS accuracy on state errors

	Nominal, nm		Improved accuracy, nm		No position or velocity error, nm	
Direction	δ_{rms}	σ_δ	δ_{rms}	σ_δ	δ_{rms}	σ_δ
N	103.48	35.441	103.47	35.438	103.45	35.513
T	87.787	52.761	86.255	52.322	88.585	53.398
W	7.9557	4.6437	8.0022	4.6601	7.9047	4.6272

lessening the requirements for the along-track thruster. At 225 km, the thrust envelope ranges from 6.5 to 10.3 mN, or a throttle envelope of only 3.8 mN. This corresponds to a 90% reduction in maximum applied thrust and a 91% reduction in throttle range.

In addition to lower maximum thrust and a narrower thrust range at 225 km, the maximum dynamic thruster response is also significantly lower. If the control acceleration requires a rate of change in applied thrust greater than the given thruster can achieve, the required acceleration will not be attained, driving state errors to increase. For a 160 km orbit, the maximum response for the along-track thruster is 41 mN/s, whereas, for a 225 km orbit, that value is reduced by a factor of 10. Whether larger dynamic responses can be achieved is dependent on the thruster system on the spacecraft. If no flow rate changes are needed, as is assumed in this study, adjustment of discharge voltage should provide sufficient throttling rate to achieve the responses predicted in this study.

The maximum power requirements for a 160 km orbit are upward of 2.2 kW, whereas, for a 225 km orbit, the maximum power is less than 200 W. Depending on the desired mission lifetime and power processing capability, this may be a crucial factor in determining mission feasibility. From a thruster standpoint, these results support finding that a 225 km orbit (still quite low by most standards) is a much more feasible environment for such a drag-free mission, based on the proposed control design and thruster models.

For a GRACE follow-up mission, lower altitude orbits may be desired for more accurate gravity mapping, however, state errors are much greater, which may effect the gravity measurements. At 225 km, the orbital altitude is less than half of GRACE's initial orbital altitude, and the maximum displacement errors are on the order of hundreds of nanometers in both the along-track normal direction. Higher accuracy spacecraft position and velocity data from the onboard GPS, if available, would still not reduce state errors significantly. However, by increasing the frequency of the ephemeris update, position and velocity errors are shown to be reduced by upward of 80% in the normal direction. When both improvements are implemented, state errors can be further reduced. It is clear that, with this controller configuration, more frequent updates on the spacecraft's position and velocity are crucial in decreasing state errors, as compared with increasing the accuracy of these data.

For the controller/thruster configuration considered, predicted mission lifetime is based on propellant consumption. Assuming an initial propellant mass of 87 kg, a 160 km altitude mission would use that amount of propellant in approximately 0.76 years. That prediction is extended to 2.27 years for an altitude of 225 km. To achieve a five-year gravity mapping mission like GRACE, given the same propulsion system and controller, the spacecraft would require approximately 170 kg of propellant for a 225 km orbit. More efficient thrusters and firing schemes (control of mass-flow rate and discharge voltage) may improve mass consumption rate but, as an initial estimate, this analysis provides an estimate of what can be expected in terms of mission lifetime and thruster requirements.

Acknowledgments

This work was supported in part by the NASA Jet Propulsion Laboratory. The authors would like to thank W. Folkner of Jet Propulsion Laboratory for many valuable suggestions. The authors would also like to thank N. Gatsonis of Worcester Polytechnic Institute for his guidance of the direct simulation Monte Carlo analysis.

References

[1] Staff of Space Dept., Johns Hopkins Univ. Applied Physics Lab., and Staff of Guidance and Control Lab., Stanford Univ., "A Satellite Freed of All but Gravitational Forces: 'TRAID 1'," *Journal of Spacecraft and Rockets*, Vol. 11, No. 9, Sept. 1974, pp. 637–644. doi:10.2514/3.62146

[2] Turneaure, J. P., Everitt, C. W. F., Parkinson, B. W., Bardas, D., and Breakwell, J. V., "The Gravity-Probe-B Relativity Gyroscope Experiment: Development of the Prototype Flight Instrument," *Advances in Space Research*, Vol. 9, No. 9, 1989, pp. 29–38. doi:10.1016/0273-1177(89)90005-7

[3] St. Rock, B., Blandino, J. B., and Demetriou, M. A., "Propulsion Requirements for Drag-Free Operation of Spacecraft in Low Earth Orbit," *Journal of Spacecraft and Rockets*, Vol. 43, No. 3, May–June 2006, pp. 594–606. doi:10.2514/1.15819

[4] Vallado, D. A., *Fundamentals of Astrodynamics and Applications*, Space Technology Library, Microcosm Press, El Segundo, CA, 2001, pp. 550–553.

[5] Hedin, A. E., "Extension of the MSIS Thermospheric Model into the Middle and Lower Atmosphere," *Journal of Geophysical Research*. Vol. 96, No. A2, 1991, pp. 1159–1172. doi:10.1029/90JA02125

[6] Gatsonis, N. A., Maynard, E. P., and Erlandson, R. E., "Monte Carlo Modeling and Analysis of Pressure Sensor Measurements During Suborbital Flight," *Journal of Spacecraft and Rockets*, Vol. 34, No. 1, Jan.–Feb. 1997, pp. 83–91.

[7] Chamberlin, R. E., and Gatsonis, N. A., "Numerical Modeling of Gas Expansion from Microtubes," *4th International Conference on Nanochannels, Microchannels and Minichannels*, American Society of Mechanical Engineers Paper ICNMM2006-96120, 2006.

[8] Ioannou, P. A., and Sun, J. H., *Robust Adaptive Control*, Prentice–Hall, New York, 1995.

[9] Manzella, D., Oh, D., and Aadland, R., "Hall Thruster Technology for NASA Science Missions," *AIAA/ASME/SAE/ASEE Joint Propulsion Conference and Exhibit*, AIAA Paper 2005-3675, 2005.

[10] Jacobson, J. T., and Jankovsky, R. S., "Test Results of a 200W Class Hall Thruster," *AIAA Joint Propulsion Conference and Exhibit*, AIAA Paper 98-3792, 1998.

[11] Ziemer, J. K., Gamero-Castano, M., Hruby, V., Spence, D., Demmons, N., McCormick, R., Roy, T., Gasdaska, C., Young, J., and Connolly, B., "Colloid Micro-Newton Thruster Development for the ST7- DRS and LISA missions," *AIAA/ASME/SAE/ASEE Joint Propulsion Conference and Exhibit*, AIAA Paper 2005-4265, 2005.

[12] Wirz, R., Gale, M., Mueller, J., and Marrese, C., "Miniature Ion Thrusters for Precision Formation Flying," *AIAA/ASME/SAE/ASEE Joint Propulsion Conference and Exhibit*, AIAA Paper 2004-4115, 2004.

[13] Zhang, S. P., and Shepherd, G. G., "Neutral Winds in the Lower Thermosphere Observed by WINDII During the April 4–5 1993 Storm," *Geophysical Research Letters*, Vol. 27, No. 13, 2000, pp. 1855–1858.

C. Kluever
Associate Editor